Shock Waves (2011) 21:523–532
DOI 10.1007/s00193-011-0338-7

ORIGINAL ARTICLE

Near-wall imaging using toluene-based planar laser-induced fluorescence in shock tube flow

J. Yoo · D. Mitchell · D. F. Davidson · R. K. Hanson

Received: 2 March 2011 / Revised: 8 August 2011 / Accepted: 20 September 2011 / Published online: 6 October 2011

Abstract A quantitative thermometry technique, based on planar laser-induced fluorescence (PLIF), was applied to image temperature fields immediately next to walls in shock tube flows. Two types of near-wall flows were considered: the side wall thermal boundary layer behind an incident shock wave, and the end wall thermal layer behind a reflected shock wave. These thin layers are imaged with high spatial resolution (15 μm/pixel) in conjunction with fused silica walls and near-UV bandpass filters to accurately measure fluorescence signal levels with minimal interferences from scatter and reflection at the wall surface. Nitrogen, hydrogen or argon gas were premixed with 1–12% toluene, the LIF tracer, and tested under various shock flow conditions. The measured pressures and temperatures ranged between 0.01 and 0.8 bar and 293 and 600 K, respectively. Temperature field measurements were found to be in good agreement with theoretical values calculated using 2-D laminar boundary layer and 1-D heat diffusion equations, respectively. In addition, PLIF images were taken at various time delays behind incident and reflected shock waves to observe the development of the side wall and end wall layers, respectively. The demonstrated diagnostic strategy can be used to accurately measure temperature to about 60 μm from the wall.

Communicated by K. Hannemann.

J. Yoo · D. Mitchell · D. F. Davidson (✉) · R. K. Hanson
High Temperature Gasdynamics Laboratory,
Department of Mechanical Engineering, Stanford University,
Stanford, CA 94305, USA
e-mail: dfd@stanford.edu

Present Address:
D. Mitchell
Department of Mechanical Engineering, Monash University,
Melbourne, Australia

Keywords Near-wall imaging · Toluene tracer · Planar laser-induced fluorescence

1 Introduction

Planar laser-induced fluorescence (PLIF) is a non-intrusive imaging technique that can instantaneously and quantitatively measure key flow parameters such as temperature, pressure, density, and species concentration in multiple spatial coordinates. PLIF techniques have been used to visualize mixing in gaseous flows as well as a diagnostic in combustion studies [1–4]. In shock tube studies, PLIF techniques have been used to image supersonic flow over a blunt body [5] and shock-induced ignition [6]. Tracers used in PLIF studies vary depending on the application at hand. Recent studies have employed a variety of tracers, including acetone [7], nitric oxide [8], OH [9], 3-pentanone [10], and toluene [11]. Compared to other ketone and aromatic tracers, toluene is an ideal candidate for quantitative thermometry due to its high temperature sensitivity in the 300–900 K range [12]. Also, toluene has a broad excitation spectrum in the near-UV allowing relatively simple excitation via commercially available laser sources.

Quantitative PLIF imaging using the toluene photophysical data presented in Koban et al. [12] was first demonstrated in a heated turbulent free jet by Luong et al. [13]. The first experiments in a shock tube were done by Yoo et al. [11], measuring temperatures in the core flow behind incident and reflected shock waves. These measurements required additional toluene fluorescence yield data at sub-atmospheric pressures, which the authors provided. Results were also reported for shock-heated flow past a wedge, with validation using numerical calculations [11]. Good agreement was

found in all regions of the flow, except near the wedge wall where viscous effects may play a role.

In this study, two regions of non-uniform temperature distribution, the thermal boundary layer on the shock tube side wall behind an incident shock wave, and the thermal layer on the shock tube end wall following shock reflection, are probed. Both regions possess significant temperature gradients between the colder wall surface and the hotter core flow, with no pressure variation. The lack of pressure variation makes these flows ideal candidates for demonstrating the applicability of this PLIF diagnostic technique.

Measurements are validated using relevant computational models. Several assumptions were made to simplify each analysis. For side wall temperatures, we assumed a laminar boundary layer and temperature-independent thermodynamic properties. The latter assumption is a good first-order approximation for the relatively narrow range of temperatures relevant to this study. Under these assumptions, the 2-D Navier–Stokes energy equation becomes a linear function and the temperature distribution can be expressed as a superposition of two components: wall plate cooling and viscous dissipation in the momentum boundary layer. Both components are shown on the right-hand side of Eq. (1), where u and v are the velocity components in the x and y directions, α the thermal diffusivity, ν the kinematic viscosity, and c_p is the heat capacity at constant pressure.

$$u\frac{\partial T}{\partial x} + v\frac{\partial T}{\partial y} = \alpha\frac{\partial^2 T}{\partial y^2} + \frac{\nu}{c_p}\left(\frac{\partial u}{\partial y}\right)^2. \tag{1}$$

This equation can be further simplified by adopting the self-similar variable, η, from the Blasius equation. The simplified equation can be solved numerically for all Prandtl numbers. It can even be solved analytically if $Pr = 1$ [14]. The Prandtl number determines the thickness of the thermal boundary layer with respect to the momentum boundary layer. For fluids with Prandtl number less than unity, the thermal boundary layer is thicker than its momentum counterpart [15]. The opposite is true for fluids with Prandtl number greater than unity.

Test gas behind the reflected shock ideally comes to rest, creating uniform temperature and pressure conditions ideal for wide varieties of scientific and engineering application. The quiescent gas near the end wall is cooled by heat transfer to the end wall, assuming no chemical reaction takes place. Since there is no bulk motion of the gas, the heat transfer in the test section is dominated by diffusion [16]. The temperature distribution of the gas near the end wall can be modeled using the 1-D heat equation, shown in Eq. (2).

$$\frac{\partial}{\partial x}\left(k_\mathrm{g}\frac{\partial T_\mathrm{g}}{\partial x}\right) = \rho c_\mathrm{p}\frac{\partial T_\mathrm{g}}{\partial t}, \tag{2}$$

where T_g is the gas temperature, k_g is the thermal conductivity, ρ is the density. This partial derivative equation can be solved numerically with variable thermal properties (α, ν, and c_p). Thermal properties of the end wall were assumed to be constant, since the temperature variation within the end wall will be very small compared to the test gas (on the order of a few degrees).

In the span of 60 years since key experimental evidence of boundary layers was reported by Dryden [17], near-wall imaging techniques have made steady progress. Various attempts to image near surfaces using traditional line-of-sight visualization technique, such as shadowgraph, schlieren, or interferometry, have met with difficulties, owing particularly to the challenge of propagating collimated light close to walls with minimal specular and diffusive (scattering) reflection from the nearby surface. Also, the aforementioned techniques are unable to resolve complex 3-D flow features [18]. Optical diagnostics that utilizes fluorescence or Raman scattering, with light collection orthogonal to a narrow plane of laser illumination, can circumvent both issues. As an additional benefit, the excitation laser wavelength used to perform these diagnostics is spectrally separated from the resulting fluorescence, resulting in smaller interference from the excitation wavelength. Near-wall flow measurements using PLIF [19–22] and Raman spectroscopy [23] have been previously demonstrated in other flows. The closest reported measurement capability was about 0.2 mm [24] from the nearby surface.

The current study details the development of a technique to image boundary layer temperature distributions and measure boundary layer development near the side and end walls of a shock tube, with a goal of determining diagnostic accuracy and capability near walls.

2 Experimental setup

2.1 Shock tube and imaging setup

Measurements were performed in the imaging shock tube at Stanford University. The shock tube has a 3-m driver section with 15-cm internal diameter and a 9.6-m driven section with 11-cm internal diameter, separated by a polycarbonate diaphragm placed between the driven and driver sections. The driven section is followed by a 2-m long recovery section, that transitions smoothly from round to square cross-section of 10 cm × 10 cm with rounded corners of $R = 1.8$ cm (holding the cross-sectional area fixed). At the end of the recovery section is an 18-cm transition to the test section with straight corners. This section gives the shock wave some distance to stabilize after the sudden change in cross-sectional area. The test section is located at the very end of the shock tube.

A wide range of shock conditions can be replicated by varying the shock strength or initial driven section conditions. Detailed information on shock tube operations can be

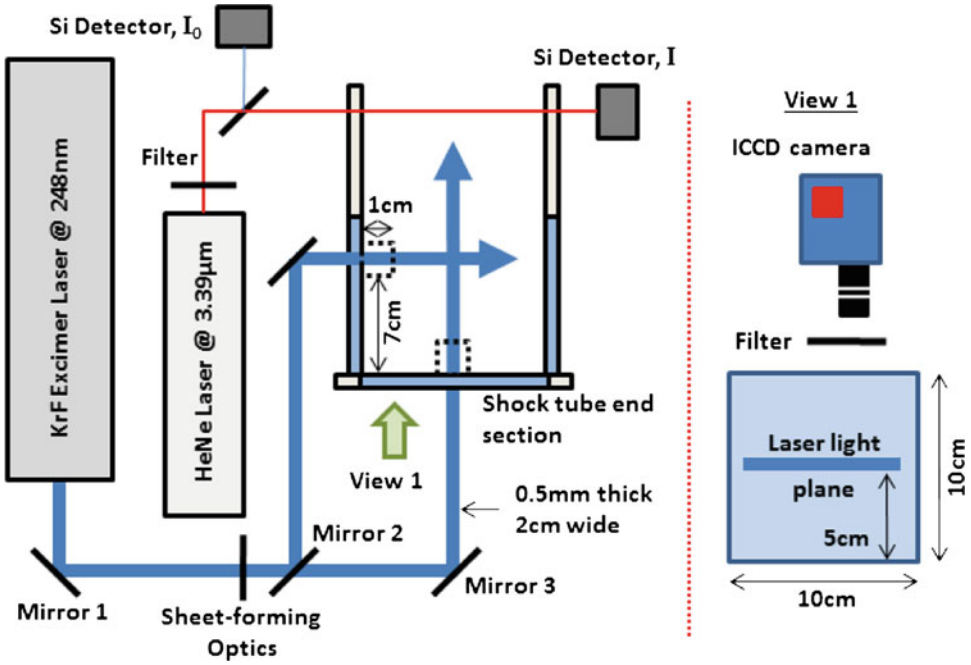

Fig. 1 Schematic of the shock tube and experimental setup. Mirror 2 deflects the laser beam to enter the test section through the side or the end wall window

found in [25,26]. The test gas is mixed with the PLIF tracer species, toluene, in a stainless steel mixing assembly using a magnetically driven stirring vane and uniformly heated to approximately 330 K. Mixtures were made manometrically using capacitance manometers and pre-shock toluene concentrations in the shock tube were confirmed using in situ 3.39 μm laser absorption measurements [27]. A series of pressure transducers placed at known locations on the shock tube were used to measure the speed of the incident shock. This information, along with initial driven section conditions, was used to calculate the core flow conditions behind the incident and reflected shock waves. Windows in the shock tube test section were designed to image flows across the entire width of the shock tube. The shock tube end section is fully transparent on three side walls ($10 \times 10 \times 1.25$ cm^3 side wall windows) and the end wall ($10 \times 10 \times 2.5$ cm^3 end wall window). Incident laser light can be accepted through any of these windows.

For PLIF measurements, a Coherent KrF excimer (COMPEX pro 102) laser outputting pulses (20 ns) of up to 250 mJ/pulse at 248 nm was used. This wavelength offers high PLIF signal temperature sensitivity while keeping the experimental setup relatively easy to configure. Laser energy was limited to 125 mJ/cm^2 to prevent fluorescence signal saturation (deviation from linear at this energy level was less than 5%). The laser beam was passed through long focal length beam-shaping optics and an iris to form an approximately 2 cm wide and 0.75 mm thick horizontal sheet. The pulse-to-pulse laser energy variation was monitored with a photodiode (LaVision). Fluorescence signals were collected through the top window and focused with a 105 mm (focal length) f/4.5 achromatic UV-lens (Nikon). The signals were imaged onto an intensified CCD camera (LaVision Dynamight, 1,024 × 1,024 pixels, 13 μm/pixel). The intensifier is gated for 150 ns, long enough to collect most of the fluorescence from the toluene tracer.

2.2 Near-wall imaging

One of the key goals in this study was to achieve reliable quantitative PLIF measurements as close to the surface as possible. This was accomplished by minimizing laser–surface interactions, mainly reflection and scatter, which may introduce significant measurement error close to the surface and even damage sensitive optics. Several wall materials, optical components, and their configurations were analyzed to optimize the experimental facility as shown in Fig. 1.

2.2.1 Wall material

Wall materials considered in this study include two metals, aluminum and steel, and one non-metal, amorphous fused silica. Surface finishes considered for aluminum and steel are #2B mill, #3, #4 satin, and #8 mirror. Fused silica surfaces treated with and without anti-reflective coating were examined. Laser-surface interactions were tested by aiming the laser sheet perpendicularly into a wall sample with the camera placed at a right angle to the sheet. Sample surfaces were cleaned and inspected thoroughly to ensure no bulk particulate or surface contamination. Tests were performed in atmospheric air at room temperature. Experimental results showed significant differences in the amount of scattered light at the

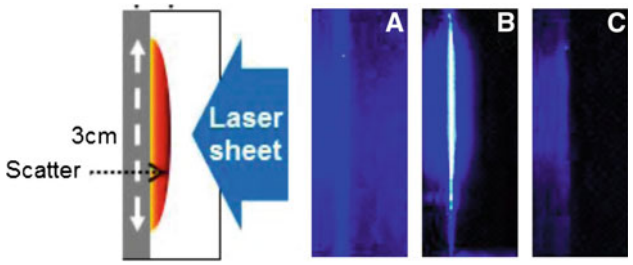

Fig. 2 Laser light scatter comparison for different wall types and optical filters in air at atmospheric pressure and room temperature. The schematic on the *left* depicts the location of sample material (shown as *grey*) in the image, scatter (shown as *red*), and laser sheet orientation. *A* Fused silica using 248 nm notch filter; *B* aluminum #8 using 248 nm notch filter; *C* fused silica using 250–400 nm bandpass filter. Images were collected at a right angle to the laser sheet

surface between materials. While metallic samples showed similar amounts of scattered light at the surface, fused silica samples showed significantly less. Examples of laser–surface interaction of fused silica and aluminum are shown in Fig. 2 (image A and B, respectively). In addition, surface finish was observed to have a negligible effect on the amount of scattered light, regardless of material, for the finishes tested. Overall, fused silica produced the least amount of surface scatter, and was selected as the wall material. Fused silica has additional benefits in that it is stiffer than its metallic counterparts, minimizing plastic deformation thereby preventing the wall from flexing as a result of shock tube operation.

2.2.2 *Optical configuration*

The amount of surface scatter observed is greatly affected by the optical arrangement. Careful consideration and proper selection of optical components and their configuration can significantly reduce or even eliminate surface scatter from reaching the camera. Surface scatter is caused by surface topography, surface contamination, bulk index fluctuation, and bulk particulates [28]. Optical filters, laser sheet polarization, laser sheet orientation and incident angle, and collection angle were varied to find the optimal optical configuration for the purpose of near-wall PLIF imaging. The laser sheet orientation refers to the direction of the input laser sheet with respect to the test section and the laser sheet incident angle refers to the angle it forms with respect to the incident window.

The electromagnetic wave orientation, or polarization, can have a significant impact on surface scatter. A Rochon prism polarizer was placed between a fused silica sample and beam-shaping optics to test two states of laser sheet polarization and their effects on surface scatter. While noticeable reduction in surface scatter was observed for one polarization over the other, it was not enough to avoid the use of an optical filter.

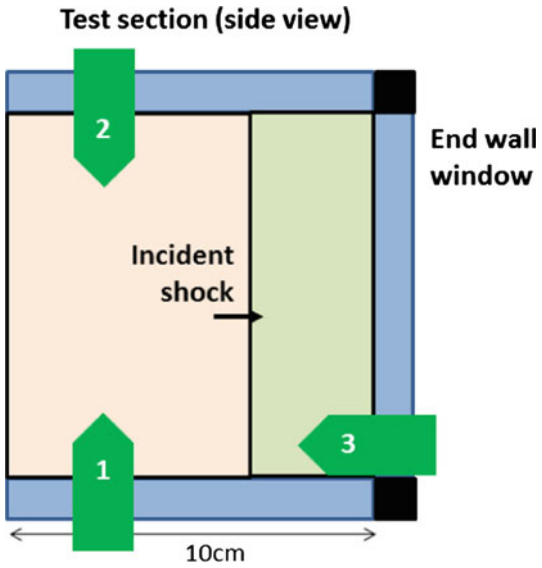

Fig. 3 Schematic of the laser sheet orientation configuration with respect to the wall and near-wall flow phenomenon. *1* Bottom-up, *2* top-down perpendicular orientation, *3* parallel orientation. Shock tube end wall is located to the right of the schematic

Spectral separation between the excitation laser wavelength (248 nm) and the toluene emission spectra (260–400 nm) permitted the use of an optical filter to selectively reject surface scatter at the excitation laser wavelength. A notch filter (centered at 248 nm) and a band-pass (250–400 nm) filter was tested in this study and the results are shown in Fig. 2 (image A and C). Small amounts of scatter still penetrate the notch filter. This is because the bandwidth of the notch filter (∼0.7 nm) is smaller than the linewidth of the excitation laser (∼1 nm). The band-pass filter almost does away with surface scatter (since the filter blocks the excitation laser wavelength) allowing more accurate quantitative analysis closer to the surface.

The unique design of the test section permits laser sheet orientations in three configurations: two perpendicular and one parallel orientation. The two perpendicular configurations are called the bottom-up orientation and the top-down orientation depending on the laser sheet routing configuration with respect to the surface of interest as shown in Fig. 3. Bottom-up and top-down perpendicular orientations are denoted as 1 and 2, respectively and the parallel orientation is denoted as 3 with respect to the surface of interest.

It is possible to completely eliminate surface scatter using carefully aligned parallel orientation. However, toluene absorption reduces the incident laser flux (as much as 15% under certain conditions) before reaching the imaging field. Also, minute diaphragm pieces and large dust particles can prevent uniform laser sheet illumination, especially at longer test times. Perpendicular orientations, despite the unavoidable surface scatter, provide more robust illumination

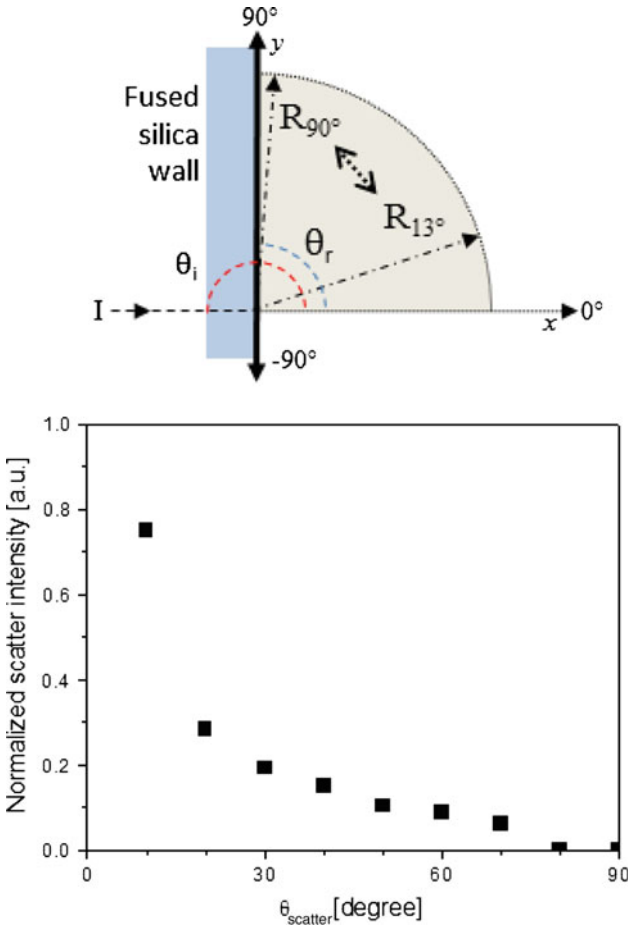

Fig. 4 *Top* Schematic of an incidence angle and various collection angles with respect to the fused silica window in cylindrical coordinate. Only the limits of the collection angle are shown. *Bottom* Normalized surface scatter from fused silica at various collection (R_1 through R_9) in the *XY*-plane at normal incidence ($\theta_i = 180°$)

in the imaging field. Of the two perpendicular orientations, the bottom-up orientation outperforms the top-down orientation on two accounts. First, the former delivers more flux in the imaging field simply due to the fact that the imaging field is attached to the incident wall of interest. Second, the bottom-up orientation eliminates specular reflection at the surface since the laser is traveling from a material with higher optical density (fused silica) to that of lower optical density (test gas). The opposite is true for the top-down orientation, wherein the incident wall reflects the specular reflection back into the imaging field. Specular reflection from a fused silica ($n \sim 1.5$) window is about 4%, which is significant enough to affect temperature measurement uncertainty.

The final step in near-wall image optimization was focused on reducing the amount of surface scatter by adjusting the laser sheet incident angle and the collection angle. A schematic describing the collection angle with respect to the normal laser sheet incidence is shown in Fig. 4. Two types of experiments are performed for this study. First, the camera was fixed in place at $\theta_r = 90°$, while the incident laser sheet was tilted in grazing angles about normal incidence ($\theta_i = 180 \pm 5°$). Results from this experiment showed very little differences in the level of surface scatter. Second, the camera was tilted from $\theta_r = 13°$ to 90° while the incident laser sheet was fixed at normal incidence ($\theta_i = 180°$). The results from the second experiment are shown in Fig. 4 (right). For materials with an isotropic surface, as was the case for fused silica, scatter peaks at the incident angle and decreases as collection angle moves away from the incident angle. The least amount of surface scatter for normal incidence ($\theta_i = 180°$) is observed near $\theta_r = 90°$. The PLIF diagnostic is optimized in accordance with these experiments. Results of boundary layer studies using the PLIF diagnostic are discussed next.

3 Results

3.1 Side wall thermal boundary layer

An incident shock wave heats and induces motion towards the end wall in the test gas. As a result, the post-shock gas in close proximity to the side walls develops a momentum and thermal boundary layer. The leading edge of the boundary layer is attached to the incident shock wave. A boundary layer can be further classified as laminar or turbulent with the transition taking place around $Re_{crit} = 5 \times 10^5$. For the shock conditions and gases (H_2, N_2, and Ar) tested in this study, the maximum Reynolds number at the end of the test time (arrival of the reflected shock) is about $Re_{max} \approx 2 \times 10^5$, indicating that the side wall boundary layer would likely remain laminar throughout the experiment, a period of roughly up to 400 μs. Depending on the test gas, the thermal boundary layer thickness can be up to 2 mm in thickness at the end of the test time.

A sample PLIF image and the corresponding temperature field at the side wall are shown in Fig. 5. These images were taken roughly 200 μs after the incident passed by the imaging field. Core flow conditions are $T = 346$ K, $P = 0.15$ bar, $U_\infty = 400$ m/s, in H_2 with 4% toluene. These values were calculated using normal shock wave equations. A well-defined thermal boundary layer is clearly visible in both images in Fig. 5. A horizontal profile across the center of the temperature image about 7.5 cm away from end wall is shown in Fig. 6 along with the predicted temperature profile calculated using theory. The side wall surface temperature was assumed to be at room temperature due to the short time scale and the thermal properties of the fused silica window. Temperature measurement accuracy within the side wall boundary layer is about ±5 K.

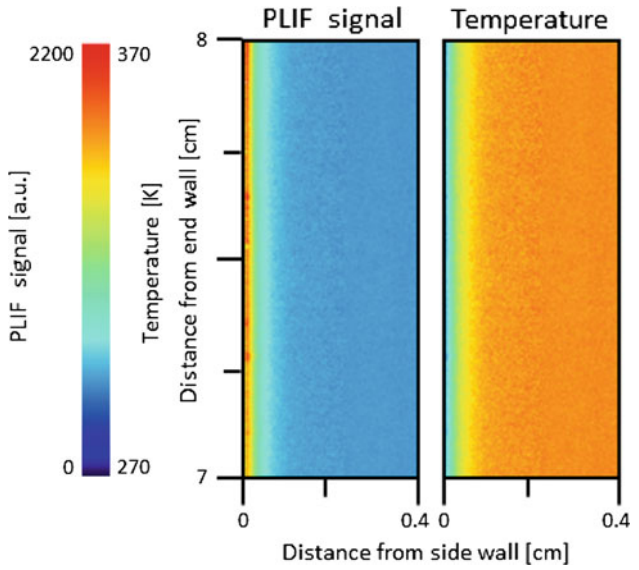

Fig. 5 (*Left*) Side wall thermal boundary layer PLIF signal and (*right*) temperature image. Shock conditions are $P_1 = 0.08$ bar, $T_1 = 293$ K, test gas: H_2 with 4% toluene, $V_s = 1{,}030$ m/s, and incident shock attenuation = 0.7%/m. Conditions in the core flow are $T_2 = 346$ K, $P_2 = 0.144$ bar, and $U_\infty = 400$ m/s. The incident shock flow travels in the downward direction. The incident shock wave passed out of the lower end of the image field 200 μs before, and thus the image shows the thermal boundary layer at a location from 20.6 to 21.6 cm behind the incident shock wave

Thermal boundary layer thicknesses from the measured and predicted temperature profiles are 1.16 and 1.21 mm, respectively (a difference of 4.7%). Boundary layer thickness was defined as the distance from the wall at which the normalized temperature θ ($=^{T-Tw}/_{T_\infty - Tw}$) is 99%, where T_w and T_∞ represent wall and core flow temperature, respectively [29].

Development of the side wall boundary layer can be visualized by taking series of images at different times behind the incident shock wave (with carrier gas H_2) with a fixed camera. A sample image constructed from five separate images taken at 10 μs intervals is shown in Fig. 7. Note that these images were not taken sequentially in a single experiment, but from five separate images under the same flow conditions. The core flow temperature and pressure variations are less than 1 and 3%, respectively, for all five images, but with different time delays. Since the shock wave speed is relatively constant for each of the five separate images, 10 μs delay in time directly corresponds to about 1 cm delay in distance. The false color scheme in Fig. 7 is scaled to easily visualize the boundary layer and its development with respect to the distance from leading edge. Figure 7 has been treated to seamlessly stitch the five separate images together. The incident shock and region 1 is visible at the far right end of the image. The shock-heated gas is flowing from left to right at a rate of about 610 m/s. The temperature and pressure behind the incident shock are 375 K and 0.15 atm, respectively. The incident shock speed is approximately 850 m/s. The boundary layer is seen to begin growing immediately behind the incident shock.

The side wall thermal boundary layer thickness for various shock conditions in N_2 and toluene test gas is shown with corresponding theoretical results in Fig. 8. The boundary layers develop proportionally to the square root of distance behind the incident shock, coinciding with conclusions drawn from the laminar boundary layer theory. The larger error bars are due to the limited spatial resolution of the PLIF image; in the present experiments, the thermal boundary layer only

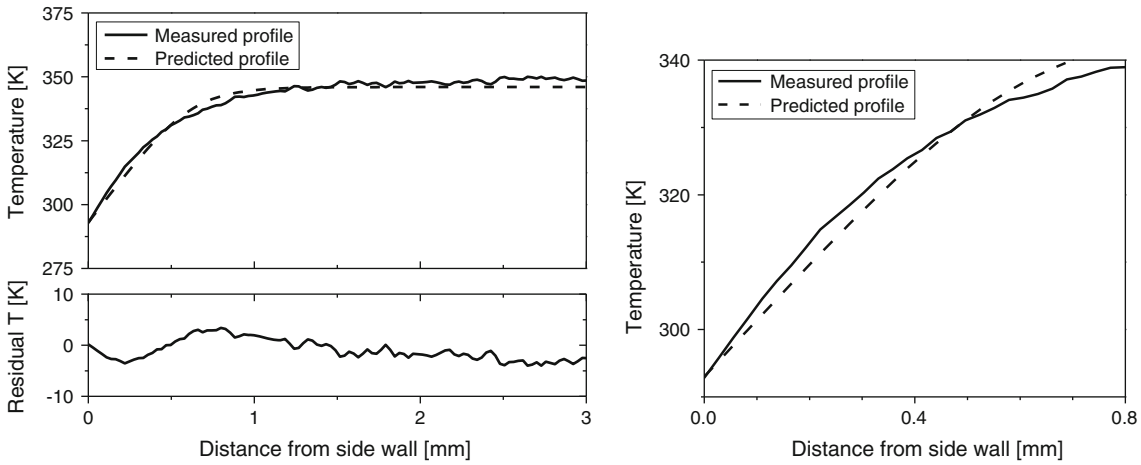

Fig. 6 *Top left* Measured and simulated temperature profile 7.5 cm away from the end wall in Fig. 5 (21.1 cm behind the incident shock wave). The measured profile is an average of a five pixel wide row horizontally across the temperature image at its center. *Bottom left* Residual temperature (between predicted and measured temperatures) profile. Conditions in the core flow are listed under Fig. 5. *Right* A detailed view of the temperature profiles near the side wall

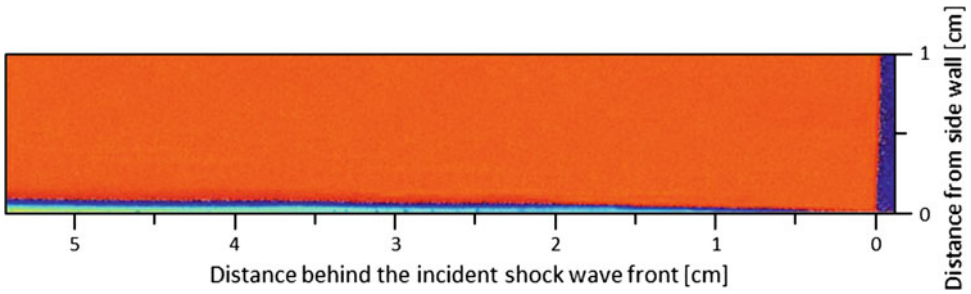

Fig. 7 Continuous thermal boundary layer visualization. The image was constructed from five different PLIF signal images taken 10 μs apart in succession. The image color scheme was adjusted to highlight boundary layer development with respect to distance behind incident shock wave front. Initial conditions are $T_1 = 293$ K, $P_1 = 0.02$ bar, 6% toluene in H_2. Core flow conditions are $T_2 = 345$ K, $P_2 = 0.04$ bar

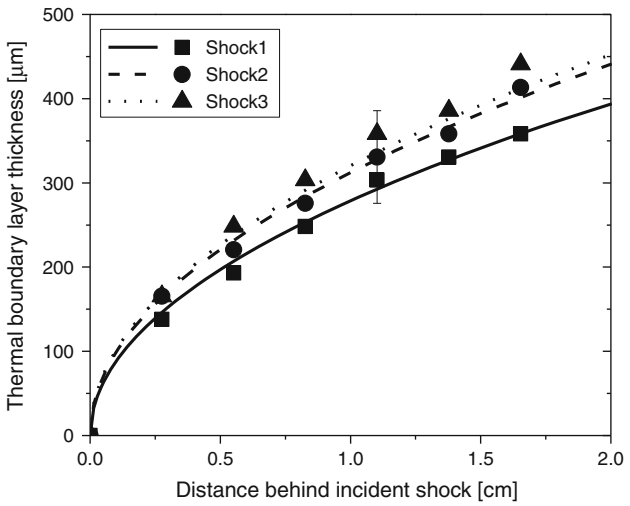

Fig. 8 Side wall thermal boundary layer thickness behind incident shocks with respect to shock strength. Initial pressure was varied from $P_1 = 0.933$ to 3.07 kPa to produce shocks in $T_1 = 293$ K and N_2 bath gas. *Lines* are calculations from boundary layer theory. Flow conditions behind each shock are listed in Table 1

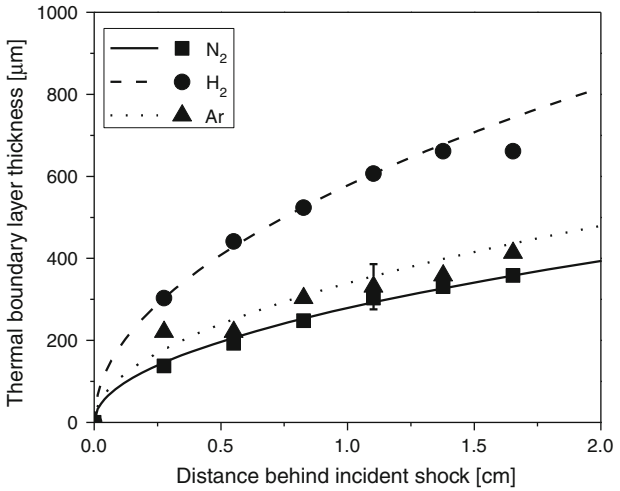

Fig. 9 Side wall thermal boundary layer thickness behind incident shocks in N_2, H_2, and Ar bath gas. Initial conditions are $P_1 = 0.933$ kPa and $T_1 = 293$ K. *Lines* are theoretical calculations from boundary layer theory. Toluene mole fraction in all three shocks was about 8.5%. Flow conditions behind each shock are listed in Table 2

Table 1 List of core flow conditions behind incident shocks given in Fig. 8. Carrier gas is N_2

	Shock 1	Shock 2	Shock 3
Pressure (bar)	0.09	0.14	0.16
Temperature (K)	400	580	550
Toluene mole fraction (%)	8.5	4.5	2.6
Free stream velocity (m/s)	735	608	492

Table 2 List of core flow conditions behind incident shocks given in Fig. 9

	N_2	H_2	Ar
Pressure (bar)	0.09	0.025	0.11
Temperature (K)	400	375	860
Free stream velocity (m/s)	735	440	700

accounts for about 50 pixels width (2% of an image) at maximum thickness. The list of core flow conditions behind incident shocks given in Fig. 8 are listed in Table 1. The side wall thermal boundary layer thickness was defined as the distance from the wall at which the normalized temperature θ ($=^{T-Tw}/_{T_\infty - Tw}$) is 99%, where T_w and T_∞ represent wall and core flow temperature, respectively.

Development of the thermal boundary layer thickness in different bath gases (N_2, H_2, and Ar) was also measured. Initial conditions for the three test cases were $P_1 = 0.933$ kPa and $T_1 = 293$ K. The list of core flow conditions behind incident shocks in Fig. 9 are listed in Table 2. Thermal boundary layer thicknesses for all three gases develop proportionally to the square root of distance behind the incident shock.

Nitrogen (N_2) was chosen for its slower incident shock speed (600–850 m/s) (when compared to lighter gases at similar Mach numbers), effectively increasing the test time

duration (up to 400 μs). In addition, nitrogen has relatively low heat capacity (c_p) and therefore is capable of reaching higher temperatures, up to 500 and 800 K behind the incident and reflected shock waves respectively, for lower Mach numbers. As a tradeoff, relatively low viscosity of nitrogen leads to thinner boundary layers. Hydrogen (H_2) produces the thickest thermal boundary layer among the three tested gases. This is because kinematic viscosity of hydrogen is an order of magnitude higher than that of nitrogen or argon despite having the fastest (850–1,200 m/s) shock wave speed for a given Mach number. However, hydrogen has very high c_p and relatively low incident shock wave Mach number (for a given driver/driven pressure ratio) which leads to smaller increases in temperature and pressure behind the incident shock wave. Temperatures behind the incident and reflected shock waves only reach to 350 and 450 K, respectively, in the current experiments. Argon was chosen due to the interest in shock tube performances. Argon is often used as a buffer gas in high-purity chemical kinetic experiments. These experiments require very uniform temperature distributions for high precision measurements. By understanding the extent of non-uniform regions (for example boundary layers) in the test gas, facility-related errors can be reduced, thereby improving chemical kinetic measurements. Argon has similar boundary layer thickness as nitrogen, but with much higher shock wave speed and therefore higher temperatures behind the incident and reflected shock waves for a given driver/driven pressure ratio.

3.2 End wall thermal layer

When an incident shock reaches the end wall, it is reflected and reheats the test gas. The twice-heated gas ideally comes to rest and heat transfer to the walls cools nearby gases. The end wall thermal layer exists unperturbed for a much longer period of time compared to the side wall thermal boundary layer, typically up to tens of milliseconds in our facility. It is disrupted by the arrival of the expansion or compression wave reflected from the contact surface. A sample PLIF and the corresponding temperature field at the end wall are shown in Fig. 10.

These images were taken about 2.3 ms after the shock reflection at the end wall. Core flow conditions are $T = 368$ K, $P = 0.19$ bar, and H_2 with 3% toluene. These values were calculated using normal shock wave relations. A well-defined thermal layer is clearly visible in both images in Fig. 10. A vertical temperature profile with respect to the distance from the end wall across the temperature image along with the predicted temperature profile is shown in Fig. 11. The measured and predicted profiles in Fig. 11 agree relatively well. The predicted temperature profile was calculated by numerically solving the heat equation and corresponding boundary conditions (i.e. assuming a wall fixed at room temperature) given in the previous section. As a result of the end wall thermal layer, the temperature at the window surface can be up to 5 K higher than the room temperature. The difference in the core flow temperature is about 1% (363.5 and 367 K for the measured and predicted profile, respectively), which falls within the temperature measurement uncertainty given in [11]. Temperature measurement accuracy within the end wall thermal layer was about ±5 K. The thermal layer thicknesses from the measured and predicted temperature profiles is 2.9 and 3.01 mm, respectively (a difference of 3.8%).

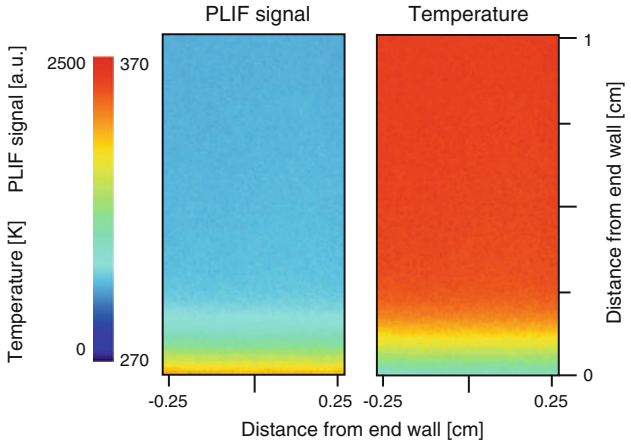

Fig. 10 (*Left*) End wall thermal layer PLIF signal and (*right*) temperature image. Shock conditions are $P_1 = 8.0$ kPa, $T_1 = 296$ K, bath gas: H_2, with 3% toluene, $V_s = 1{,}010$ m/s. Image was taken about 2.3 ms after shock reflection. Core flow conditions behind reflected shock are $T_5 = 368$ K, $P_5 = 0.19$ bar. The reflected shock travels in an upward direction

Identifying the end wall thermal layer development is important in chemical kinetics studies where knowledge of temperature and pressure is paramount. This can be accomplished by making measurements as close to the end wall as possible while staying clear of the end wall thermal layer. A combination of shock strength and initial conditions was chosen to produce the thickest thermal layer possible using the existing experimental facility to quantify its region of influence. Several tests were performed at various time delays after shock reflection to visualize end wall thermal layer development as shown in Fig. 12.

The end wall thermal layer thickness develops proportionally to the square root of time, for times much greater than $Pe^{-1/2} \ll 1$ [30]. Where V_R is the reflected shock velocity, and α is the thermal diffusivity of gas behind a reflected shock and $Pe = V_R^2/\alpha$. (Péclet number) is a dimensionless number that is defined as the ratio of advection to the rate of diffusion of the test gas. The EWTL thickness was defined as the distance from the wall at which the normalized temperature θ ($=^{T-Tw}/_{T_\infty - Tw}$) reaches 99%, where T_w and T_∞ represent wall and core flow temperature, respectively. The solid line in Fig. 12 is the best square root fit to

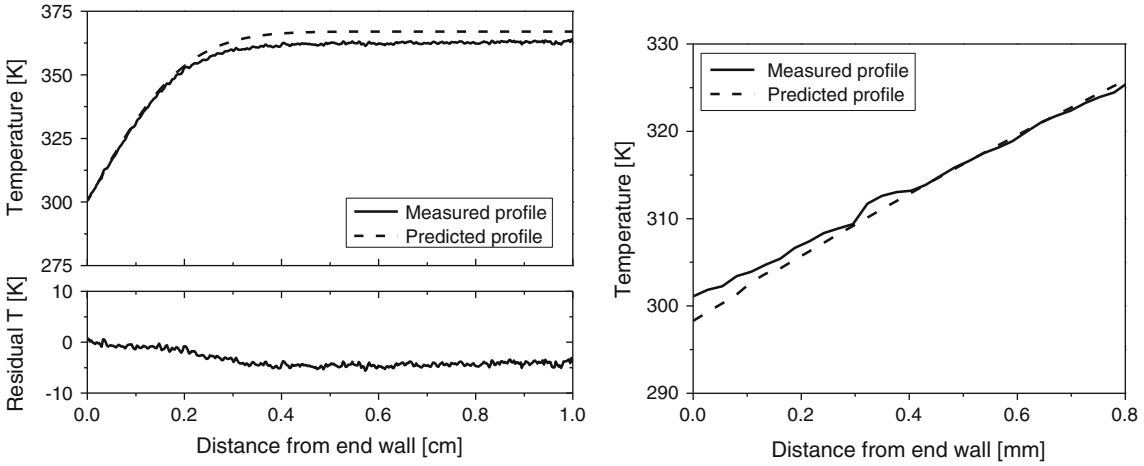

Fig. 11 *Top left* Measured and predicted temperature profile along the center of temperature image in Fig. 10. Measured profile is an average of a five pixel wide column across the entire height of the image. *Bottom left* Residual temperature (between predicted and measured temperatures) profile. Shock conditions and core flow conditions are mentioned above. Initial conditions and core flow conditions behind reflected shock is given under Fig. 10. *Right* A detailed view of the temperature profiles near the end wall

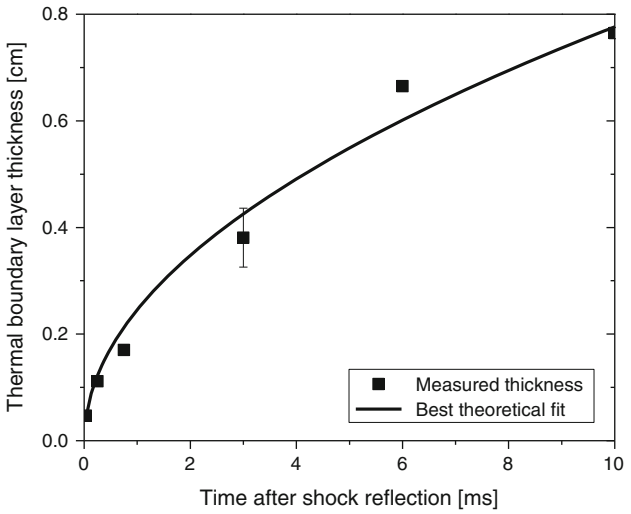

Fig. 12 End wall thermal layer thickness behind a reflected shock. Initial conditions are $T_1 = 293$ K and $P_1 = 0.14$ bar, bath gas: H_2, with 1.5% toluene $V_s = 1{,}100$ m/s. *Solid lines* are theoretical best fit from boundary layer theory. Conditions in the core flow behind the incident shock are $T_5 = 340$ K and $P_5 = 0.24$ bar

the data. The measured end wall thermal layer continues to develop until about 12 ms after shock reflection, and levels off until about 22 ms. At that time, the arrival of the expansion or compression wave reflected from the contact surface disrupts the thermal layer uniformity.

4 Conclusion

A quantitative temperature-field measurement technique based on toluene PLIF was used to image non-uniform temperature fields near walls behind the incident and reflected shock waves in shock tube flows. 2-D images taken with high spatial resolution were found to be relatively free of laser-surface interaction if proper optical arrangement and filters are used. Temperature measurements near both the side and end walls agreed with predicted results from relevant theories, exhibiting measurement uncertainty of about ±5 K. The side wall thermal boundary layer and end wall thermal layer development measurements agreed well with theory. In the future, this diagnostic technique could be used to identify pockets of local temperature variation in shock tube experiments with chemical reactions behind the incident or reflected shock waves. This diagnostic technique could also be extended to monitor pressure and tracer number density through the use of multiple excitation wavelengths or detectors.

Acknowledgments This work was supported by the Department of Energy (National Nuclear Security Administration) under Award Number NA28614 and by the Air Force Office of Scientific Research (AFOSR) Aerospace, Chemical and Material Science Directorate, Combustion and Diagnostics section with Dr. Julian Tishkoff as program manager.

References

1. Hanson, R.K.: Combustion diagnostics: planar flowfield imaging. Proc. Combust. Inst. **21**, 1677–1691 (1986)
2. Kohse-Hoinghaus, K., Jeffries, J.B.: Applied Combustion Diagnostics. Taylor and Francis, London (2002)
3. Kychakoff, G., Howe, R.D., Hanson, R.K.: Quantitative flow visualization technique for measurements in combustion gases. Appl. Optics **23**, 704–712 (1984)
4. Wolfrum, J.: Lasers in combustion: From basic theory to practical devices. Proc. Combust. Inst. **27**, 1–41 (1998)
5. McMillin, B.K., Lee, M.P., Hanson, R.K.: Planar laser-induced fluorescence imaging of shock-tube flows with vibrational nonequilibrium. AIAA **30**, 436–443 (1992)

6. McMillin, B.K., Lee, M.P., Paul, P.H., Hanson, R.K.: Planar laser-induced fluorescence imaging of shock-induced ignition. Proc. Combust. Inst. **23**, 1909–1913 (1990)
7. Lozano, A., Yip, B., Hanson, R.K.: Acetone: a tracer for concentration measurements in gaseous flows by planar laser-induced fluorescence. Exp. Fluids **13**, 369–376 (1992)
8. Seitzman, J.M., Kychakoff, G., Hanson, R.K.: Instantaneous temperature field measurements using planar laser-induced fluorescence. Opt. Lett. **10**, 439–441 (1985)
9. Seitzman, J.M., Hanson, R.K., DeBarber, P.A., Hess, C.F.: Application of quantitative two-line OH planar laser-induced fluorescence for temprally resolved planar thermometry in reacting flows. Appl. Optics **33**, 4000–4012 (1994)
10. Neij, H., Johansson, B., Alden, M.: Development and demonstration of 2D-LIF for studies of mixture preparation in SI engines. Combust. Flame **99**, 449–457 (1994)
11. Yoo, J., Mitchell, D., Davidson, D.F., Hanson, R.K.: Planar laser-induced fluorescence imaging in shock tube flows. Exp. Fluids (2010). doi:10.1007/s00348-010-0876-2
12. Koban, W., Koch, J.D., Hanson, R.K., Schulz, C.: Absorption and fluorescence of toluene vapor at elevated temperatures. Phys. Chem. Chem. Phys. **6**, 2940–2945 (2004)
13. Luong, M., Koban, W., Schulz, C.: Novel strategies for imaging temperature distribution using toluene LIF. JPCS **45**, 133–139 (2006)
14. Kakac, S., Yener, Y.: Convective Heat Transfer. CRC Press, Boca Raton (1995)
15. Incropera, F.P., DeWitt, D.P., Bergman, T.L., Lavine, A.S.: Introduction to Heat Transfer. Wiley, New York (2007)
16. Onishi, Y.: On flows behind shock waves reflected from a solid wall. Shock Waves **1**, 293–299 (1991)
17. Dryden, H.L.: Air flow in the boundary layer near a plate. T.R. No 682, N.A.C.A. (1972)
18. Houwing, A.F.P., Smith, D.R., Fox, J.S., Danehy, P.M., Mudford, N.R.: Laminar boundary layer separation at a fin-body junction in a hypersonic flow. Shock Waves **11**(1), 31–42 (2001)
19. Smith, J.D., Sick, V.: Crank-angle resolved imaging of biacetyl laser-induced fluorescence in an optical internal combustion engine. Appl. Phys. B **81**, 579–584 (2005)
20. Fajardo, C.M., Smith, J.D., Sick, V.: Sustained simultaneous high-speed imaging of scalar and velocity fields using a laser. Appl. Phys. B **85**, 25–31 (2006)
21. Pfefferle, L.D., Griffin, T.A., WinterDavid, M., Crosley, R., Dyer, M.J.: The influence of catalytic activity on the ignition of boundary layer flows part I: hydroxyl radical measurements. Combust. Flame **76**(3–4), 325–338 (1989)
22. Schrewe, M.R., Ghandhi, J.B.: Near-wall formaldehyde planar laser-induced fluorescence measurements during HCCI combustion. Proc. Combust. Inst. **31**, 2871–2878 (2007)
23. Taschek, M., Egermann, J., Schwarz, S., Leipertz, A.: Quantitative analysis of the near-wall mixture formation process in a passenger car direct-injection Diesel engine by using linear Raman spectroscopy. Appl. Opt. **44**(31), 6606–6615 (2005)
24. Hultqvist, A., Engdar, U., Johansson, B.: Reacting boundary layers in a homogeneous charge compression ignition (HCCI) engine. SAE Trans. **110**, 1086–1098 (2001)
25. Hanson, T.: The development of a facility and diagnostics for studying shock-induced behavior in micron-sized aerosols. Doctoral Dissertation, Stanford University (2005)
26. Haylett, D.R., Lappas, P.P., Davidson, D.F., Hanson, R.K.: Application of an aerosol shock tube to the measurement of diesel ignition delay times. In: Proc. Combustion. Inst. **32**, 477–484 (2009)
27. Klingbeil, A.E., Jeffries, J.B., Hanson, R.K.: Temperature-dependent mid-IR absorption spectra of gaseous hydrocarbons. J. Quant. Spectrosc. Radiat. Transf. **107**, 407–420 (2007)
28. Stover, J.C.: Optical Scattering: Measurement and Analysis. McGraw-Hill, New York (1990)
29. Schlichting, H., Gersten, K.: Boundary Layer Theory. Springer, Berlin (2000)
30. Sturtevant, B., Slachmuylders, E.: End-wall heat-transfer effects on the trajectory of a reflected shock wave. Phys. Fluids **8**(8), 1201–1207 (1964)